

See discussions, stats, and author profiles for this publication at: <https://www.researchgate.net/publication/270217911>

# Diazole-based powdered cocrystal featuring a helical hydrogen-bonded network: Structure determination from PXRD, solid-state NMR and computer modeling

ARTICLE *in* SOLID STATE NUCLEAR MAGNETIC RESONANCE · DECEMBER 2014

Impact Factor: 2.27 · DOI: 10.1016/j.ssnmr.2014.12.005

---

CITATIONS

2

READS

171

---

## 8 AUTHORS, INCLUDING:



Mariana Sardo

University of Aveiro

28 PUBLICATIONS 176 CITATIONS

[SEE PROFILE](#)



Artem A Babaryk

National Taras Shevchenko University of Kyiv

28 PUBLICATIONS 26 CITATIONS

[SEE PROFILE](#)



Concepción López

National Distance Education University

95 PUBLICATIONS 1,084 CITATIONS

[SEE PROFILE](#)

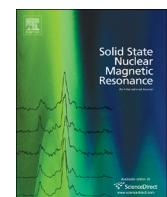


Rosa M Claramunt

National Distance Education University

472 PUBLICATIONS 5,632 CITATIONS

[SEE PROFILE](#)



# Diazole-based powdered cocrystal featuring a helical hydrogen-bonded network: Structure determination from PXRD, solid-state NMR and computer modeling

Mariana Sardo <sup>a</sup>, Sérgio M. Santos <sup>a</sup>, Artem A. Babaryk <sup>a,b</sup>, Concepción López <sup>c</sup>, Ibon Alkorta <sup>d</sup>, José Elguero <sup>d</sup>, Rosa M. Claramunt <sup>c,\*\*</sup>, Luís Mafra <sup>a,\*</sup>

<sup>a</sup> Department of Chemistry, CICECO, University of Aveiro, 3810-193 Aveiro, Portugal

<sup>b</sup> Faculty of Chemistry, Taras Shevchenko National University of Kyiv, Volodymyrska s. 64/13, 01601 Kyiv, Ukraine

<sup>c</sup> Departamento de Química Orgánica y Bio-Orgánica, Facultad de Ciencias, UNED, Senda del Rey 9, E-28040 Madrid, Spain

<sup>d</sup> Instituto de Química Médica (CSIC), Juan de la Cierva 3, E-28006 Madrid, Spain

## ARTICLE INFO

### Article history:

Received 6 October 2014

Accepted 7 December 2014

### Keywords:

Cocrystal

Diazole

NMR Crystallography

Crystal engineering

Hydrogen bond network

C-H · · · π interactions

Solid-state NMR

## ABSTRACT

We present the structure of a new equimolar 1:1 cocrystal formed by 3,5-dimethyl-1H-pyrazole (**dmpz**) and 4,5-dimethyl-1H-imidazole (**dmim**), determined by means of powder X-ray diffraction data combined with solid-state NMR that provided insight into topological details of hydrogen bonding connectivities and weak interactions such as C-H · · · π contacts. The use of various 1D/2D <sup>13</sup>C, <sup>15</sup>N and <sup>1</sup>H high-resolution solid-state NMR techniques provided structural insight on local length scales revealing internuclear proximities and relative orientations between the **dmim** and **dmpz** molecular building blocks of the studied cocrystal. Molecular modeling and DFT calculations were also employed to generate meaningful structures. DFT refinement was able to decrease the figure of merit  $R(F^2)$  from ~11% (PXRD only) to 5.4%. An attempt was made to rationalize the role of N-H · · · N and C-H · · · π contacts in stabilizing the reported cocrystal. For this purpose four imidazole derivatives with distinct placement of methyl substituents were reacted with **dmpz** to understand the effect of methylation in blocking or enabling certain intermolecular contacts. Only one imidazole derivative (**dmim**) was able to incorporate into the **dmpz** trimeric motif thus resulting in a cocrystal, which contains both hydrophobic (methyl groups) and hydrophilic components that self-assemble to form an atypical 1D network of helicoidal hydrogen bonded pattern, featuring structural similarities with alpha-helix arrangements in proteins. The 1:1 **dmpz** · · · **dmim** compound **I** is the first example of a cocrystal formed by two different azoles.

© 2014 Elsevier Inc. All rights reserved.

## 1. Introduction

Although complete crystal structure determination can be achieved through well-established powder X-ray diffraction (PXRD) methods, complementary structural information increases the success rate, confidence level and accuracy of the final structure [1]. For this purpose, NMR crystallography combines the high sensitivity of solid-state (SS) NMR to local structural details, the accuracy in detecting long-range ordering and crystal symmetries shown by XRD and the potential of first-principles calculations to correlate several computed and experimental parameters.

Structure determination of small molecules from PXRD is not a trivial task and is significantly more challenging than from single-crystal XRD data. In fact, contributions performing crystal structure determination of powdered multicomponent crystals, such as the imidazole–pyrazole cocrystal system we present in this work, are still scarce. Moreover, the comparison between calculated and experimental SSNMR parameters has been performed within the crystal structure prediction (CSP) of small organic molecules mainly in the case of previously known structures, where SSNMR data is used for the selection and quality assessment of the final structures [2,3]. A recent publication based on CSP methods applied to a drug molecule [4] tried to obtain the crystal structure without previous knowledge from other techniques. However, many authors do not attempt to validate their results with PXRD and it is known that different crystal packing arrangements may give rise to very similar chemical shifts (CSs) and there the relying exclusively in the CSs for structure validation may be incautious. Structure validation with PXRD combined with SSNMR and DFT

\* Corresponding author.

\*\* Corresponding author.

E-mail addresses: [rclarum@ccia.uned.es](mailto:rclarum@ccia.uned.es) (R.M. Claramunt), [lmafra@ua.pt](mailto:lmafra@ua.pt) (L. Mafra).

methods will also ensure that we have much less chances of observing a local minima structure. For example, a recent contribution from Dudenko and co-workers determined the structure of the cocrystal of indomethacin and nicotinamide from PXRD, assessing the validity and quality of the determined structure against experimental and calculated  $^1\text{H}$  and  $^{13}\text{C}$  SSNMR CSs [5].

The development of the powerful GIPAW-DFT approach for periodic solids [6,7] has enabled an unprecedented matching between measured and computed CS values when calculations are performed on highly accurate crystal structure models [8,9]. Although the analysis in terms of  $^{13}\text{C}/^{15}\text{N}$  CSs is regarded as a valuable tool for assessing the quality of XRD structure solutions [5,10], other parameters, such as  $^1\text{H}$  CSs [11,12], torsion angle restraints [13], intermolecular distances [14] or  $^1\text{H}-^1\text{H}$  distances [15], represent a more direct approach to crystal structure determination on powders. In fact,  $^1\text{H}$  NMR parameters are well suited for the purpose of crystal structure validation since the level of calculation is more accurate for  $^1\text{H}$  spins and  $^1\text{H}$  is also an interface nucleus, much more sensitive to packing interactions present in the supramolecular arrangements of organic solids.

The potential of SSNMR and GIPAW calculations of  $^1\text{H}$  CSs in the field of cocrystal engineering has generated recent interest due to its capability in discerning between distinct H-bond connectivities on similar structures [5,16,17]. Cocrystals exhibit long-range order and their multiple components interact via specific assemblies based upon a hierarchy of intermolecular interactions, particularly H-bonds [18]. It is of particular interest to identify and rationalize the supramolecular synthons and understand how the balance between strong and weak forces determines the precise result of cocrystal structures in the solid-state. Various weak dispersive interactions, such as  $\pi \cdots \pi$  stacking [19,20], cation  $\cdots \pi$  [21,22] and C-H  $\cdots \pi$  [23–25] contacts represent the backbone of the self-assembly process and play a significant role in shaping complex supramolecular architectures of many chemical and biological systems. However, few studies have been performed involving SSNMR studies of these intermolecular interactions. Despite the structural similarity, the physical origin of the attraction in the C-H  $\cdots \pi$  interaction (dispersion) is completely different from that of conventional H-bonds (electrostatic) [26]. Therefore, understanding the role of C-H  $\cdots \pi$  contacts is relevant as they play an important role in controlling crystal packing, increasing the stability of organic compounds and molecular recognition in both biological systems and materials [27–29]. Recently, our group has focused on the study of C-H  $\cdots \pi$  contacts detected in an anhydrate/hydrate drug system, showing they may lead to  $^1\text{H}$  shifts of approximately 3–4 ppm in the  $^1\text{H}$  NMR spectra [12].

This article reports the cocrystal formation when 3,5-dimethylpyrazole (**dmpz**) is mixed with four imidazole derivatives (Scheme 1). Pyrazoles and imidazoles are unique templates associated with several biological activities finding application in agrochemicals and new drug development [30–33]. **dmpz** was the

first reported compound to present a dynamic process in the solid-state that consists in the proton transfer along the N-H  $\cdots$  N bonds forming a trimer [34–36]. When **dmpz** is mixed (through grinding) with the different compounds in a 1:1 molar proportion (Scheme 1), only one of the compounds [4,5-dimethylimidazole (**dmim**)] reacts with **dmpz**, breaking down the aforementioned **dmpz** trimer, giving rise to a new cocrystal structure (**I**). This does not happen if **dmpz** is mixed with other  $^1\text{H}$ -imidazoles, namely: imidazole, 2-methylimidazole and 2,4(5)-dimethylimidazole (Scheme 1) [37].

In this work, we are interested in studying a new imidazole-pyrazole based cocrystal (**I**) and understanding the influence of distinct H-bonding arrangements in the construction of novel supramolecular assemblies. It is our goal to investigate about what is the supramolecular structure originated by the breaking of the stable **dmpz** H-bond trimer in the presence only of **dmim** molecules to produce **I**, since three strong N-H  $\cdots$  N bonds are initially present in the crystal lattice of **dmpz** and are disrupted and rearranged only upon reaction with one of the azoles (**dmim**). This behavior prompted us to study which type of packing interactions are involved in the transformation between both supramolecular H-bond networks. The family of the tested imidazole derivatives (Scheme 1), that play the role of cocrystal formers, is particularly interesting since they possess both hydrophobic (methyl groups) and hydrophilic components that in this case self-assemble to form an helicoidal H-bonded pattern, featuring structural similarities with alpha-helix arrangements in proteins. To pursue this goal, we have solved the crystal structure of **I** by PXRD, using DFT calculations and an ensemble of NMR techniques [high-resolution 1D  $^1\text{H}$ ,  $^{13}\text{C}$  and  $^{15}\text{N}$  as well as 2D  $^1\text{H}-^{13}\text{C}$  (PRESTO, CP and LG-CP) HETCOR and 2D  $^1\text{H}-^1\text{H}$  DQ] to help building the structure model and validate the proposed final structure. The input provided by SSNMR was particularly relevant for the validation of the crystal structure as it presents unusual proximities between hydrophobic moieties (methyl groups).

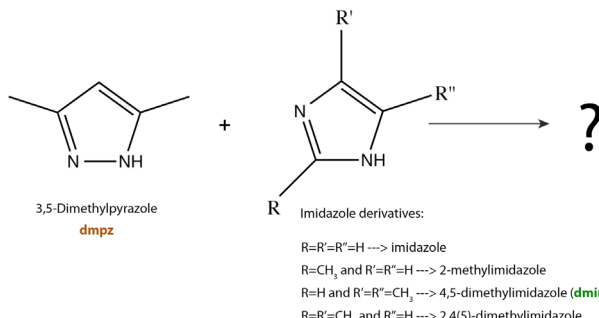
## 2. Experimental section

### 2.1. Preparation of the cocrystal

Compounds **dmpz** (99%, melting point: 105–108 °C) [38] and **dmim** (99%, melting point: 117–119 °C) [39–41] were prepared as described in the literature. **I** was prepared using two different methods: (i) both components were mixed in an agate mortar with two drops of chloroform and ground with a pestle for 10 min until a homogeneous mixture was obtained, (ii) the compounds were dissolved in ethanol (5 mL), the solvent removed in vacuum and an oil was then obtained that solidified in the refrigerator. In all cases, the stoichiometry was confirmed by means of  $^1\text{H}$  NMR solution spectroscopy.

### 2.2. Solid-state NMR experiments

The magic-angle spinning (MAS) SSNMR spectra were acquired on three different Bruker Avance III spectrometers operating at a  $B_0$  field of 9.4, 16.4 and 18.8 T, depending on the type of experiment performed (specific information provided in the corresponding figure caption). All experiments performed at  $B_0=9.4$  T were recorded at room temperature, using a double-resonance 4 mm Bruker MAS probe and a spinning rate of 10 kHz. The  $^1\text{H}$ ,  $^{13}\text{C}$  and  $^{15}\text{N}$  Larmor frequencies were 400.1, 100.6 and 40.6 MHz, respectively.  $^1\text{H}$  scaling factors were determined by comparing  $^1\text{H}$  DUMBO [42] and  $^1\text{H}$  single-pulse (at high spinning rates) spectra. The one-dimensional (1D)  $^1\text{H}$  MAS spectra was recorded on a 18.8 T spectrometer operating at the  $^1\text{H}$  Larmor frequency of



Scheme 1. Diazole compounds used to prepare possible cocrystal candidates.

800.3 MHz, on a 3.2 mm Bruker MAS probe, at a spinning rate of 24 kHz and recycle delay (RD) of 40 s. At this spinning rate the acquisition was performed at low temperature ( $< 10^{\circ}\text{C}$ ) to avoid phase transformations. All  $^1\text{H}$  CSs are quoted in ppm from TMS,  $^{13}\text{C}$  and  $^{15}\text{N}$  CSs were externally referenced to the C=O carbonyl peak (176.03) and amine peak ( $-347.6$ ) of glycine (used as secondary reference), respectively.

At  $B_0=9.4\text{ T}$ , the  $^1\text{H}$ ,  $^{13}\text{C}$  and  $^{15}\text{N}$  90° pulses were set to 3.75, 3.5 and 6.0  $\mu\text{s}$  corresponding to a radio-frequency (RF) field strength of 67, 71 and 42 kHz respectively. The  $^1\text{H}$ - $^{13}\text{C}$  CP (cross-polarization) MAS experiment was acquired using a contact time of 3.0 ms with  $^1\text{H}$  RF of 71 kHz (50–100% RAMP (ramped-amplitude)-CP shape),  $^{13}\text{C}$  RF of 69 kHz and RD of 40 s. The  $^1\text{H}$ - $^{15}\text{N}$  CPMAS experiment was acquired using a contact time of 2.0 ms with  $^1\text{H}$  and  $^{15}\text{N}$  RF of 85 kHz (50–100% RAMP-CP shape) and 42 kHz, respectively; RD=20 s. During the acquisition period, the SPINAL-64 (small phase incremental alternation, with 64 steps) [43] decoupling scheme was employed with a pulse length of 5.0 and 7.25  $\mu\text{s}$  at a RF field strength of 75 and 70 kHz, respectively for the  $^1\text{H}$ - $^{13}\text{C}$  and  $^1\text{H}$ - $^{15}\text{N}$  CPMAS experiments.

The  $^1\text{H}$ - $^{13}\text{C}$  HETCOR (heteronuclear correlation) experiment ( $B_0=9.4\text{ T}$ ) was performed using a PRESTO-II [44] magnetization transfer based on the R18 $^7$  rotor-synchronized symmetry (RF=90 kHz). Eight pairs of 180° pulses were used for the PRESTO recoupling block;  $^1\text{H}$  homonuclear decoupling during  $t_1$  was accomplished with a windowed DUMBO pulse shape using the z-rotation supercycle (wDUMBO $^{x,-x}$ ) [45] with a pulse length of 28.0  $\mu\text{s}$ ; an RF field strength of 100 kHz and 6.4  $\mu\text{s}$  windows. During the acquisition of the  $^{13}\text{C}$  signal, a SPINAL-64 decoupling with RF field strength of 75 kHz and a RD=20 s were used.

The 2D  $^1\text{H}$ - $^{13}\text{C}/^{15}\text{N}$  Lee-Goldburg (LG)-CP spectra ( $B_0=9.4\text{ T}$ ) were performed with a nutation frequency of 74 kHz (effective field of 90 kHz) for the  $^1\text{H}$  Lee-Goldburg condition with a RAMP-CP shape on  $^{13}\text{C}$  or  $^{15}\text{N}$  using a RF field strength of 100 and 90 kHz for  $^1\text{H}$ - $^{13}\text{C}$  and  $^1\text{H}$ - $^{15}\text{N}$  experiments, respectively. The LG offset irradiation during CP was set to 52972 Hz.  $^1\text{H}$  homonuclear decoupling during  $t_1$  was accomplished using wDUMBO $^{x,-x}$  with the same experimental conditions as described above. During the acquisition period, a SPINAL-64 decoupling using a pulse length for the unit pulses of 4.0 and 4.7  $\mu\text{s}$  and a RF field strength of 100 kHz and 83 kHz was employed, respectively for  $^1\text{H}$ - $^{13}\text{C}$  and  $^1\text{H}$ - $^{15}\text{N}$  HETCOR NMR experiments; RD=20 s.

The 2D  $^1\text{H}$ - $^1\text{H}$  DQ-SQ spectrum was acquired on a Bruker Avance III 700 spectrometer ( $B_0=16.4\text{ T}$ ) using a triple-resonance 2.5 mm Bruker MAS probe and a spinning rate of 26 kHz. The R16 $^2$  symmetry (RF=104 kHz) was applied for DQ excitation/reconversion and RD=20 s.

The 2D  $^1\text{H}$ - $^{15}\text{N}$  CP HETCOR spectrum ( $B_0=16.4\text{ T}$ ) was acquired using a triple-resonance 2.5 mm Bruker MAS probe and a spinning rate of 25 kHz. The  $^1\text{H}$  and  $^{15}\text{N}$  Larmor frequencies were 700.13 and 70.97 MHz, respectively. The CP step was performed with a contact time of 1.0 ms with  $^1\text{H}$  and  $^{15}\text{N}$  RF field strength of 100 kHz (50–100% RAMP-CP shape) and 40 kHz, respectively. RD=65 s. During the acquisition period, the SPINAL-64 decoupling scheme was employed with a pulse length of 4.0  $\mu\text{s}$  at a RF field strength of 80 kHz.

### 2.3. Powder X-ray diffraction

Pale-yellow powder **I** was gently mixed in an agate mortar to achieve homogeneity of the sample. About 10 mg of the resulting mixture were transferred to 1-mm borosilicate glass capillary (Hampton Research glass #50) and sealed with wax. Data acquisition was performed with Panalytical Empyrean system equipped with PIXcel position sensitive device detector with opening aperture 3.3473°, focusing mirror, 1/4° and 1/2°. Divergence and

anti-scattering slits in a primary and secondary beam. 0.02 rad. Soller slits were used to minimise axial divergence of the beam. The range 2.5–90° in  $2\theta$  was scanned with a total acquisition time of 16 h. The sample was rotated with capillary spinner at a rate of 60 rpm to increase particle statistics. Collected data were rebinned to step sizes of 0.007°. Powder pattern was indexed employing the successive dichotomy method [46,47] as implemented in DIC-VOL06 software using 13 positions of well-resolved peaks, resulting in a monoclinic cell [ $M(13)=77.6$ ,  $F(13)=92.0$  (0.0052, 27)]. Space group absences were checked by Le Bail routine in EXPO2013 suite [48] leading to P2<sub>1</sub>/c space group. For the purpose of structure solution, the initial model was constructed based on gas phase geometry and minimized with MMFF94 force field [49] with default convergence parameters.

The obtained initial geometry was used for the real-space hybrid big bang – big crunch method of structure solution [50] that is essentially an evolutionary theory type of algorithm. The global minimum of the solution was achieved by ten successive runs of the algorithm. The candidate solutions were validated through the implemented cost function  $wR=9.37\%$ , that has, particularly, the same definition as for Rietveld analysis [51]. Further Rietveld refinements were carried within GSAS program. Both **dmpz/dmim** fragments were initially treated as rigid bodies while giving free refinement of non-model based parameters, namely, scale factor, 20 terms of Chebyshev polynomial to model background, profile parameters (Thompson-Cox-Hastings profile function [52] with Howard formulation of peak asymmetry [53]), sample shift, Lorentzian components of particles size broadening/microstrain effect and its anisotropy. During the refinements, the remaining effect of preferred orientation was modeled by spherical harmonics functions up to the 8th order. Upon convergence, the model was released off rigid body description and refined normally employing individual fractional coordinates. All the operations described above were done without the presence of H-atoms, since, in respect to their scattering factors it is not possible to locate them directly from electron density maps (Fig. S1), recognized as one of the known problems for X-ray powder diffraction [54]. Hence, intermediate model converged to the  $R(F^2)=7.6\%$  was used for theoretical modeling of hydrogen atomic positions, and re-introduced to accomplish the refinements on the full model. At that stage, hydrogen atomic positions were normalized due to actual temperature of the experiment ( $T=298\text{ K}$ ) and corresponding isotropic displacement parameters (IDP's) were constrained in an assumption of  $U(\text{H})=1.2^*\text{U}(\text{C})$  for methine and  $U(\text{H})=1.5^*\text{U}(\text{C})$  for methyl group hydrogen atoms, while (IDP's) for acidic H at N atoms were refined freely in concert with full atomic array. For the sake of conciseness, all details concerning the full structural information are gathered in Tables S1–S3 (ESI). The CIF file (CCDC # 1038612) may also be found in the ESI.

### 2.4. Computer modeling methods

The calculation of NMR CSs was performed within the framework of DFT, using the plane wave pseudopotential formalism and the PBE functional [55] defined within the generalized gradient approximation. All calculations were carried out with version 6.1 of the CASTEP code [56], employing ultrasoft pseudopotentials calculated on the fly; computation of shielding tensors was performed using the GIPAW method of Pickard et al. [6,7].

The starting structure of **I** was obtained from Rietveld refinement, as described previously. An initial optimization of the atomic positions was conducted with a basis set cutoff of 60 Ry (816 eV) and a  $1 \times 2 \times 1$  Monkhorst-Pack  $k$ -point grid (corresponding to a  $k$ -point spacing of  $0.05\text{ \AA}^{-1}$ ). CASTEP default values for geometry convergence criteria were used.

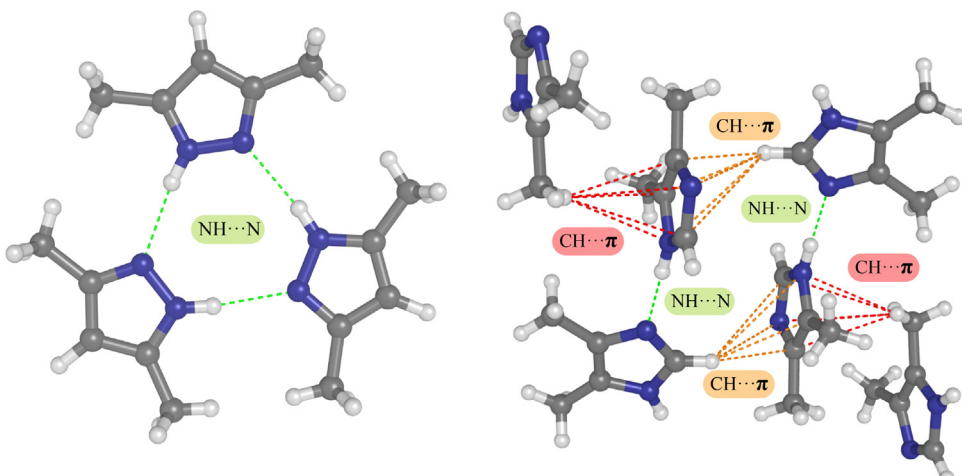


**Fig. 1.** X-ray crystal structure of **dmpz** (left, CSD code: DASXEA & DASXEA10 [57–60]) and **dmim** (right, CSD code: HABMOO [61]), highlighting selected intermolecular contacts. The **dmpz** structure contains one molecule in the asymmetric unit ( $Z=1$ ) while **dmim** contains three molecules ( $Z=3$ ).

Calculation of  $^1\text{H}$ ,  $^{13}\text{C}$  and  $^{14}\text{N}$  chemical shieldings was then undertaken on the optimized structure, using the same basis set cutoff and Monkhorst–Pack grid indicated above. Conversion of the calculated isotropic chemical shieldings ( $\sigma_{\text{iso}}$ ) into the corresponding isotropic CSs ( $\delta_{\text{iso}}$ ) was performed according to the following equation:

$$\delta_{\text{iso}} = (\sigma_{\text{iso}} - \sigma_{\text{ref}})/m \quad (1)$$

where  $\sigma_{\text{ref}}$  and  $m$  were determined by fitting  $\sigma_{\text{iso}}$  to the measured CSs ( $\delta_{\text{exp}}$ ) by means of a linear regression, being  $\sigma_{\text{ref}}$  and  $m$  the intercept and slope of the regression model, respectively.

### 3. Results and discussion

#### 3.1. Structural description

At the time we published our previous results on this system [37], only the X-ray structure of **dmpz** was known (DASXEA & DASXEA10) [57–60]. In 2010 the **dmim** structure (HABMOO) [61] has also been determined (Fig. 1). Before describing the H-bonded network formed in **I**, we briefly provide the main structural features observed in **dmpz** and **dmim** crystal structures.

The primary packing motif in imidazole-based crystals consists of N–H...N chains of heterocycles, with adjacent molecules oriented in an approximately antiparallel arrangement, enabling an extended network of linear N–H...N H-bonds with a good degree of close-packing [62]. **dmim** crystallizes with three molecules in the asymmetric unit (Fig. 1, right), with two of the molecules mutually antiparallel (173.5° rotation between the two rings) and the third is distinctly out of plane (rotated by 72.7° and 67.8° compared to the adjacent imidazoles), taking part in an interchain C–H...π interaction, electrostatically driven by the electron-rich nature of the ring compared to the protons. Overall, each H-bonded chain has become helicoidal, with both being represented in the extended structure due to the centrosymmetric space group ( $P2_1/c$ ) [62]. As mentioned before, **dmpz** presents both a H-bond donor and a H-bond acceptor site, forming trimers in the solid-state (Fig. 1, left). This structure allows the concerted transfer of the three N–H protons along the H-bonds.

Upon mixing **dmpz** and **dmim**, under the conditions described in the experimental section (either by mechanical grinding or dissolution/evaporation), they crystallize in the monoclinic  $P2_1/c$  space group with two molecule moieties in the asymmetric unit (Fig. 2), combined by intermolecular N–H...N H-bonds into

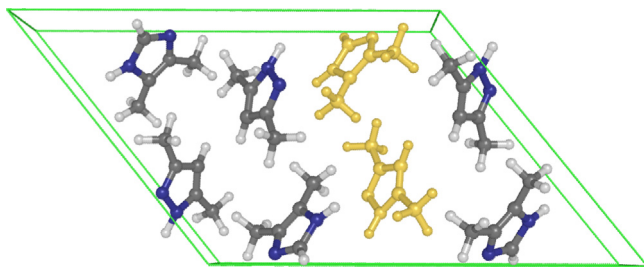


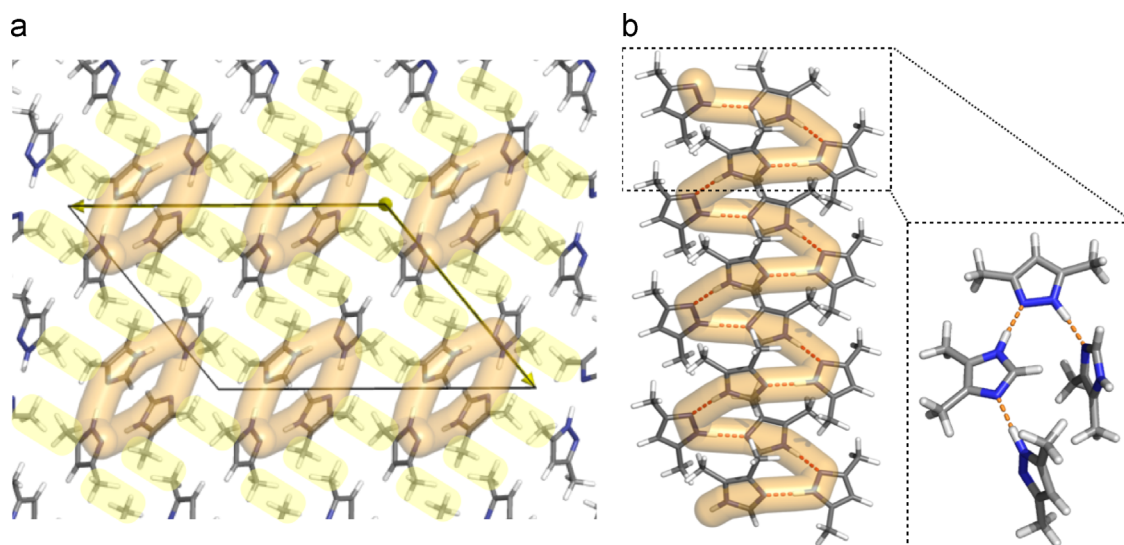
**Fig. 2.** View of the unit cell of **I**. The parent **dmpz** and **dmim** molecules in the asymmetric unit are highlighted in yellow ( $Z=1$ ). (For interpretation of the references to color in this figure legend, the reader is referred to the web version of this article.)

infinite chain-like packing along [010] direction, forming the structural motif of **I**. Fig. 3b depicts that the helicoidal arrangement of **I** is unified by two N–H...N bonds formed between one **dmpz** and two distinct **dmim** molecules. The centrosymmetric character of this group implies that the unit cell corresponds to two enantiomeric helices, the *M* and the *P*.

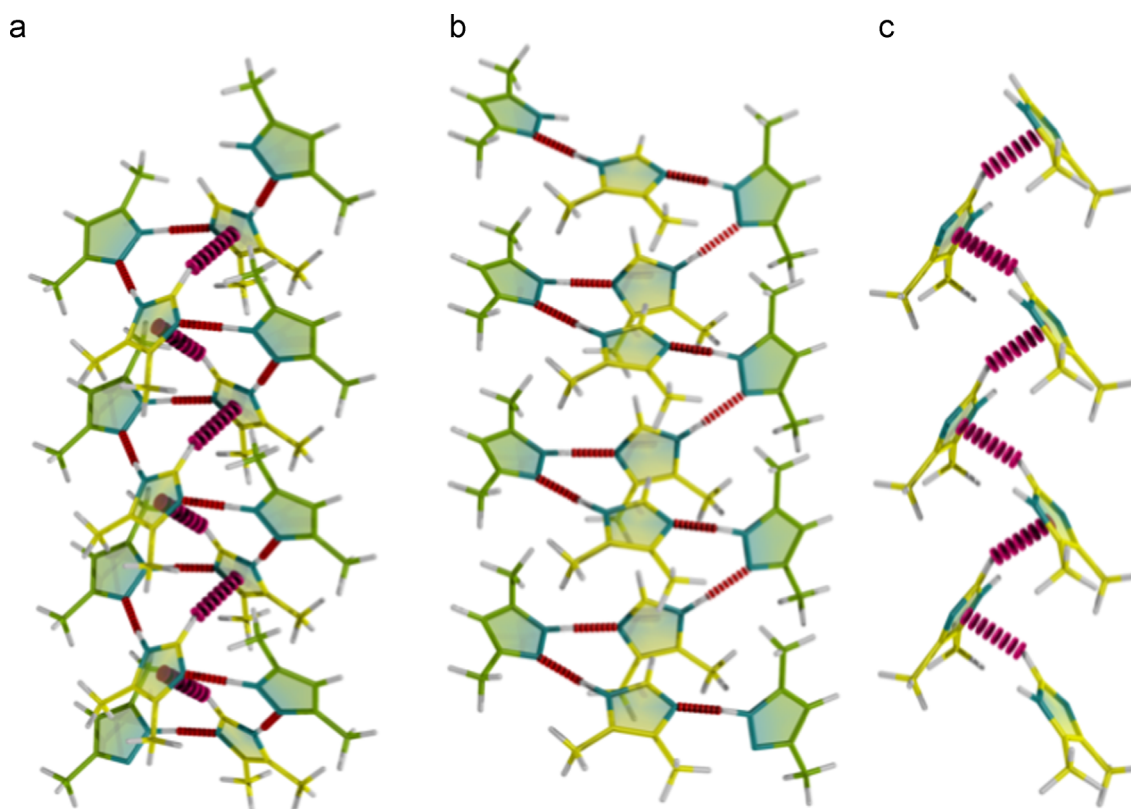
The general cocrystal cohesion is not based solely on H-bonding as it is likely expected, but it is supported by C(sp<sup>2</sup>)-H...π and C(sp<sup>3</sup>)-H...π contacts: both imidazole and pyrazole rings are potentially π-donors due to its aromatic nature, thus, another bonding pattern is recognized at view along [001] crystal axis. However, the analysis of the geometrical parameters, pointing to the interactions, suggests the existence of a dominating contribution emerging from the interactions of imidazole ring and methine proton over the much weaker contribution of that found for pyrazole ring and corresponding methyl hydrogen atoms.

Noteworthy, in the crystal structure of **I**, the C–H...π contacts described for pure **dmim** are also present between all **dmim** molecules within the cocrystal; it is thus interesting to note that such contacts are preserved upon formation of **I**.

The three core packing interactions (two N–H...N and one C–H...π, Fig. 3b) allow the formation of the helices, contributing to the cohesion and stability of the structure. This new crystal arrangement is therefore, under these experimental conditions, more stable than that of **dmim** and **dmpz** pure compounds. Fig. 4a–c shows that the **dmpz** and **dmim** monomers in **I** are interleaved along the helix (**dmim**...**dmpz**...**dmim**...**dmpz**...) through an N–H...N H-bonded helicoidal chain (Fig. 4b). The network of C–H...π contacts between all **dmim** residues is also emphasized (Fig. 4c). The structure of **I** expands along the crystallographic *b*-axis and the pitch of the helix is 6.1 Å



**Fig. 3.** (a) Expanded view across the crystal structure with some of the strongly hydrophobic regions highlighted (composed of CH<sub>3</sub> groups all facing outside the helices). The carbons in the CH<sub>3</sub> groups of opposing helices are separated by 3.75 Å. (b) Helicoidal structure of **I** with the N-H···N hydrogen bonds represented with dashed line and highlighted in orange. A detailed view of the main interactions responsible for the formation of the new cocrystal is shown on the right.

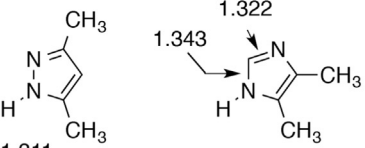
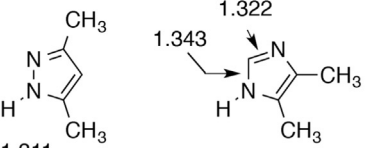
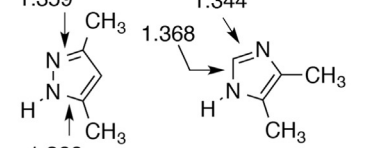
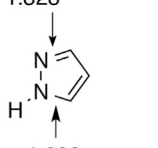
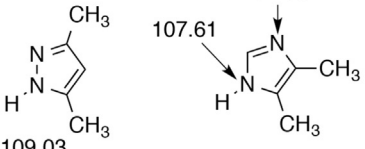
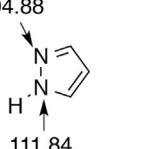
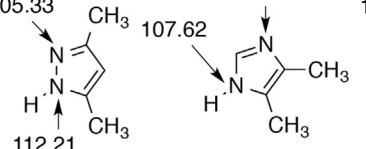
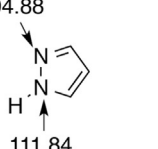


**Fig. 4.** Scheme illustrating the helicoidal network of H-bonding present in **I**. (a) both N-H···N and C-H···π interactions are represented; (b) N-H···N network highlighted with red dashed line and (c) scheme emphasizing the C-H···π interactions between **dmim** molecules in **I** (**dmpz** molecules have been omitted in this scheme for the sake of simplicity). (For interpretation of the references to color in this figure legend, the reader is referred to the web version of this article.)

(for comparison, the pitch of an  $\alpha$ -helix is 5.4 Å). Fig. S2 presents a view across the unit cell, showing several helices and their corresponding arrangements. The inter-helix regions are strongly hydrophobic as they are composed of all CH<sub>3</sub> groups from **dmim** and **dmpz** residues (detail shown in Fig. 3a).

It has been reported that the C-N distances and internal angles involving the tautomeric N atoms of pyrazoles and imidazoles, as well as those of indazoles and benzimidazoles, can be used to

determine the position of the NH proton often a difficult problem in X-ray crystallography [63–72]. We have summarized in Fig. 5 these values. In imidazoles, the distances are a better test than in pyrazoles, the contrary happens with angles that are more different in pyrazoles. In any case, the dynamic disorder present in **dmpz** (induced by NH proton exchange) leading to an equalization of distances and angles is absent in the other compounds. Cocrystal **I** resembles **dmim** on one hand and <sup>1</sup>H-pyrazole on the

	Cyclic trimer dynamic proton disorder DASXEA	Catemer HABMOO	1:1 Complex I	Catemer PYRZOL
Bond lengths	 <p>1.311 1.322 1.343</p> <p>D = 0.000 Å</p>	 <p>1.322 1.343</p> <p>D = 0.021 Å</p>	 <p>1.359 1.344 1.368 1.366 1.332</p> <p>D = 0.007 Å</p>	 <p>1.328 1.332</p> <p>D = 0.004 Å</p>
Bond angles	 <p>104.89 107.61 109.03</p> <p>D = 0.00°</p>	 <p>104.88 105.92 111.84</p> <p>D = 6.96°</p>	 <p>105.33 107.62 112.21 105.33</p> <p>D = 6.88°</p>	 <p>104.88 105.92 111.84</p> <p>D = 1.70°</p>

**Fig. 5.** Comparison of bond lengths and bond angles of **dmpz**, **dmim** and <sup>1</sup>H-pyrazole (from the CSD with their refcodes) [57–60] with those of compound **I**. Since often there are several independent molecules (between 2 and 4) in the unit cell the reported values are mean ones (with about  $\pm 0.01$  Å and  $\pm 0.1^\circ$  deviations). D is the difference between two values (note that the sign is always positive).

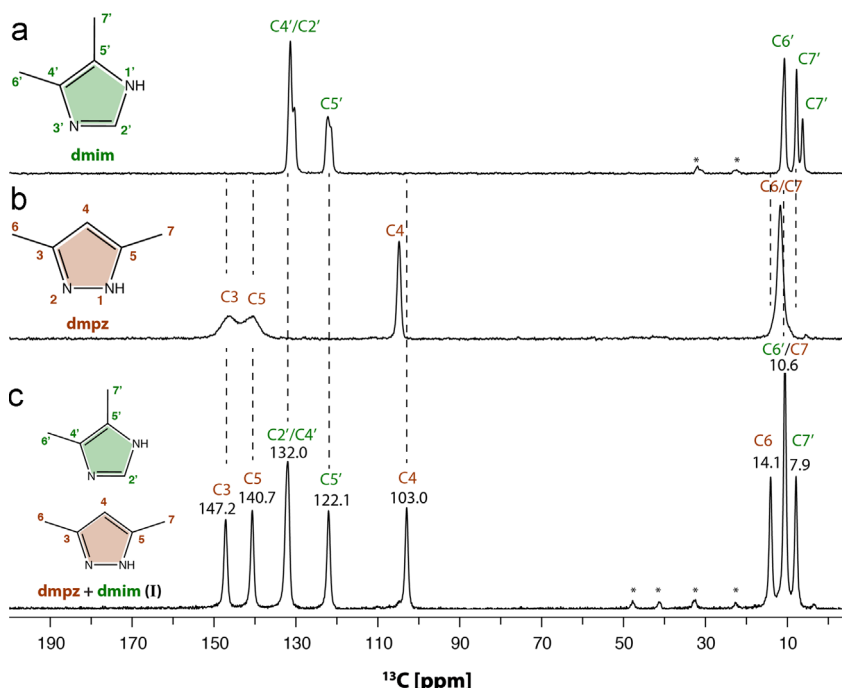


**Fig. 6.** 1D <sup>13</sup>C CPMAS NMR spectra of (a) **ddim**, (b) **dmpz** and (c) **I** recorded at  $B_0=9.4$  T with 10 kHz MAS frequency. In the case of **dmpz**, it is possible to distinguish signals arising from C3 and C5, compared to our previous results [37], where <sup>13</sup>C NMR spectra were recorded at lower  $B_0$ . The peaks marked with \* represent spinning sidebands.

other, being thus a static cocrystal. The existence or absence of dynamic disorder in **I** will be further evidenced ahead comparing <sup>13</sup>C and <sup>15</sup>N CPMAS NMR spectra of **dmpz** and **I**.

### 3.2. Solid-state NMR resonance assignment

The <sup>13</sup>C CPMAS NMR spectrum of **I** (Fig. 6c) displays eight resonances, thus suggesting the presence of a single molecule of each component in the crystallographic asymmetric unit ( $Z=1$ ). Furthermore, the broadest resonances (C3 and C5) present in the **dmpz** spectrum (Fig. 6b), are due to the proton chemical exchange involving fast proton transfer between nitrogens whose effect is propagated at the adjacent carbons. These carbon resonances

become, however, narrow in the new cocrystal [resonances at ca. 147 (C3) and 141 (C5)]. The effect observed on the <sup>13</sup>C signals of **dmpz** is similar to that reported when the spectrum is recorded at low temperatures [36], although the explanation is different; in the present case, the narrowing of these carbon lines is due to the disruption of the **dmpz** trimer while in the cited example is due to a slowing down of the proton transfer rate in the trimer. The full assignment of the <sup>13</sup>C CPMAS spectra of **ddim** and **dmpz** molecules is given in Fig. 6a and b and was supported with GIPAW-DFT CS calculations. For the case of **ddim**, the observation of seven resonances is justified by the presence of more than one molecule in the asymmetric unit. Although **dmim** has  $Z=3$  (Fig. 1, right) it is evident from the <sup>13</sup>C CPMAS spectrum that a complete

**Table 1**Experimental and GIPAW-calibrated CSs of **I** (resonances in green and brown color correspond to residues of **dmim** and **dmpz**, respectively).

Atom	$\delta_{exp}$ / ppm	$\delta_{GIPAW}$ / ppm	$\delta_{exp} - \delta_{GIPAW}$ / ppm
carbon			
2'	132	130,3	1,7
4'	132	133,5	-1,5
5'	122,1	123,7	-1,6
6'	10,6	10,1	0,5
7'	7,9	8	-0,1
3	147,2	146	1,2
4	103	104,8	-1,8
5	140,7	139,6	1,1
6	14,1	14,2	-0,1
7	10,6	10,2	0,4
Proton			
2'	4,8	4,5	0,3
6'	1,4	1,3	0,1
7'	0,7	0,8	-0,1
NH'	13	13,3	-0,3
4	5,2	5,2	0
6	1,5	1,7	-0,2
7	1,4	1,3	0,1
NH	15	14,8	0,2
Nitrogen			
1'	-207,6	-209,1	1,5
3'	-127,9	-129,3	1,4
1	-168,5	-165,5	-3
2	-99,3	-99,4	0,1

separation of all expected resonances is not possible due to signal overlap. The peaks attributed to the methyl groups (Fig. 6a) have different relative intensities since the peak at *ca.* 6 ppm (most shielded resonance) is ascribed to one methyl group (C7') attached to C5'. The resonance immediately at the left, i.e., at 7.7 ppm arises from the other two equivalent C7' methyl groups of the remaining two **dmim** molecules present in the asymmetric unit. The three crystallographically distinct C6' methyl group all appear around 10.7 ppm. The unequivocal assignment of the carbon resonances from the CH<sub>3</sub> groups of **I** is not possible based solely on this spectrum, however with the help of DFT CS calculations (Table 1), the correlations observed at 14.1 and 7.9 ppm can be attributed to the CH<sub>3</sub> groups in **dmpz** and **dmim** residues, respectively, whereas

the resonance at 10.6 ppm is assigned to CH<sub>3</sub> groups in both **dmpz** and **dmim** (this resonance is twice the intensity when compared to the other methyl resonance thus indicating the presence of two overlapped CH<sub>3</sub> groups at this CS).

The <sup>1</sup>H MAS spectra of compounds **dmpz**, **dmim** and **I**, recorded at high-field (800 MHz) are displayed in Fig. 7. The presence of strong H-bonds is easily observed for all structures as they give rise to CSs typically > 10 ppm. The spectrum of **dmpz** (Fig. 7b) and **dmim** (Fig. 7a) depict <sup>1</sup>H resonances at 14.0 and 15.3 ppm, respectively, associated to strong N-H...N hydrogen bonds (emphasized in Fig. 1). Comparatively, the spectrum of **I** (Fig. 7c) provides sufficient resolution to distinguish the two types of N-H...N interactions (13.0 and 15.0 ppm) forming the

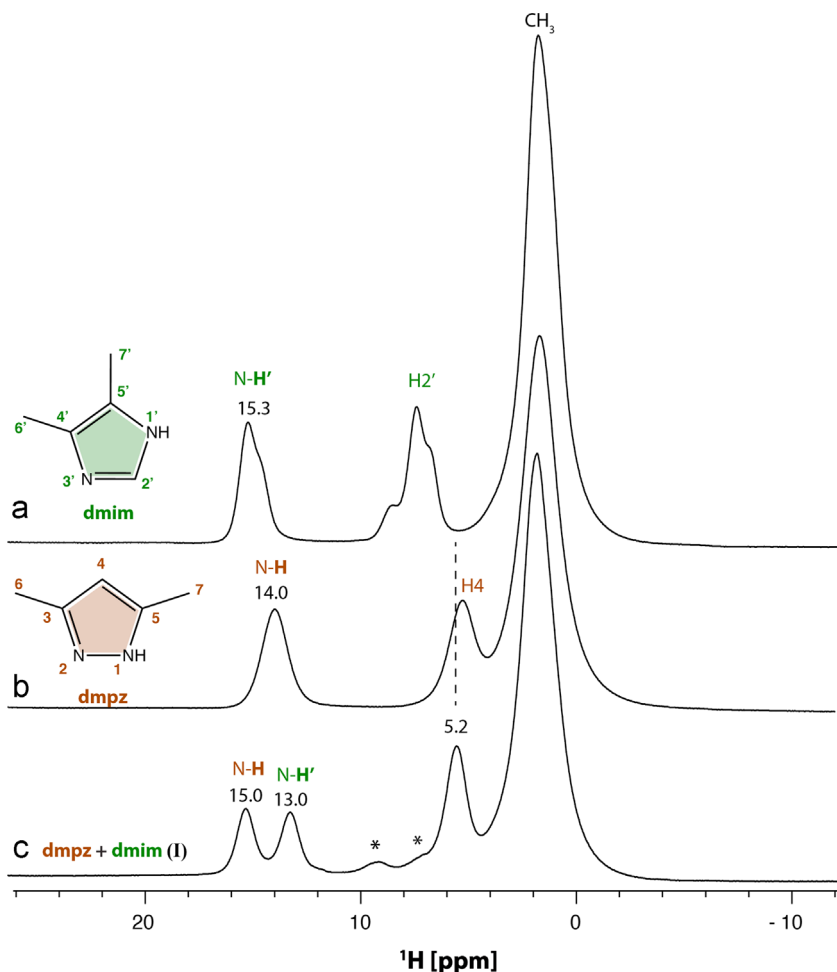


**Fig. 7.** 1D <sup>1</sup>H MAS NMR spectra of (a) **dmim**, (b) **dmpz** and (c) **I** recorded at  $B_0=18.8$  T with 24 kHz MAS frequency. The peaks marked with an asterisk appear due to sample impurities, most likely arising from **dmim**.

H-bonded helix (Figs. 3b and 4). To unambiguously assign the two strong N–H...N hydrogen bonds observed in the <sup>1</sup>H MAS NMR spectrum of **I**, GIPAW <sup>1</sup>H CS calculations (Table 1) combined with 2D <sup>1</sup>H–<sup>13</sup>C LG-CP HETCOR spectra (Fig. 12) and 2D <sup>1</sup>H–<sup>15</sup>N HETCOR (Fig. 13) were used to assign the peaks at 13.0 and 15.0 to N–H<sub>dmim</sub> (label 1' in Fig. 7a) and N–H<sub>dmpz</sub> (label 1 in Fig. 7b), respectively. From the experimental point of view, the assignment of <sup>1</sup>H resonances in **I** would not have been possible without additional NMR data as the resonances shown in **I** are, evidently, not just the sum of **dmim** and **dmpz**.

The four resonances observed in the <sup>15</sup>N CPMAS NMR spectrum of **I** (Fig. 8) can be unequivocally assigned to the four nitrogen atoms present in the cocrystal as expected, with CSs close to pure **dmpz** and **dmim** molecules. The <sup>15</sup>N resonances at –99.3 and –168.5 ppm are assigned to the N and N–H groups in **dmpz** while the –127.9 and –207.6 ppm resonances are ascribed to the same groups in the **dmim** molecule, respectively. Again, the two types of <sup>15</sup>N environments shown for **dmim** (Fig. 8a) present various resonances overlapped as its crystal structure contains more than one molecule in the asymmetric unit ( $Z'=3$ ). The assignment of <sup>15</sup>N resonances for N and N–H groups was confirmed through multiple <sup>15</sup>N CPMAS experiments recorded at different contact times and by GIPAW <sup>15</sup>N CS calculations (Table 1). It is interesting to note that the <sup>15</sup>N resonances of **dmpz** (Fig. 8b) are noticeably broadened compared to the other compounds. This effect directly reflects the fast proton transfer between N and NH species as observed for <sup>13</sup>C resonances C3 and C5 in Fig. 8b.

### 3.3. Probing intermolecular interactions using SSNMR methods

The following section deals with the discussion of SSNMR experiments evidencing intermolecular contacts able to provide distance restraints between the cocrystal molecules of **I** and aid to propose a PXRD structure model. A number of 1D (discussed in the previous section) and 2D NMR methods were performed; special emphasis is given to high-resolution <sup>1</sup>H SSNMR methods to check H-bond connectivities and relative orientation of **dmim** and **dmpz** residues within the structure of **I**.

The 2D <sup>1</sup>H–<sup>13</sup>C PRESTO-HETCOR NMR spectrum of **I** (Fig. 9), employing wDUMBO for <sup>1</sup>H–<sup>1</sup>H decoupling at the indirect dimension only shows <sup>13</sup>C...<sup>1</sup>H correlations of directly bonded protons to carbons, thus quaternary carbons are filtered out. The PRESTO block is based on an RN<sub>n</sub><sup>q</sup> rotor-synchronized symmetry-based sequence, which affords selectivity similar to that of J-mediated experiments albeit with higher sensitivity [12,44,73]. This spectral editing technique helps in the unequivocal assignment of the two through-bond <sup>1</sup>H...<sup>13</sup>C connectivities arising from the C–H groups of the **dmim** and **dmpz** moieties present in **I**:  $\delta_H=4.75$  ppm for C2' (**dmim**) and  $\delta_H=5.20$  ppm for C4 (**dmpz**). With this experiment, it is also possible to identify three distinct <sup>1</sup>H CSs associated to the CH<sub>3</sub> carbons, which can be assigned with the help of GIPAW calculations: peaks at  $\delta_H=1.5$  and  $\delta_H=0.7$  ppm ascribed to the CH<sub>3</sub> protons of **dmpz** and **dmim**, respectively, whereas the peak at  $\delta_H=1.4$  ppm is due to the overlapped contributions of CH<sub>3</sub> groups in both **dmpz** and **dmim** (both CH<sub>3</sub>

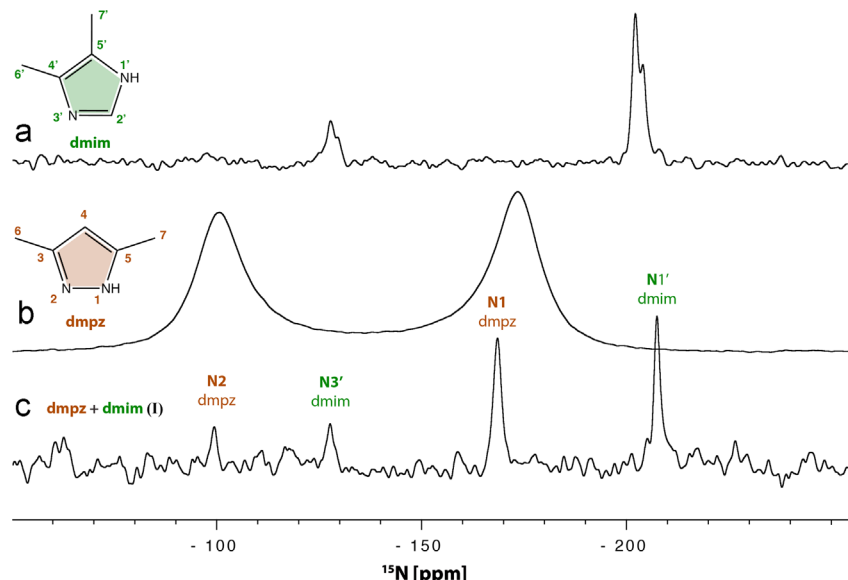


**Fig. 8.** 1D  $^{15}\text{N}$  CPMAS NMR spectra of (a) dmim, (b) dmpz and (c) I recorded at  $B_0=9.4$  T with 10 kHz MAS frequency.

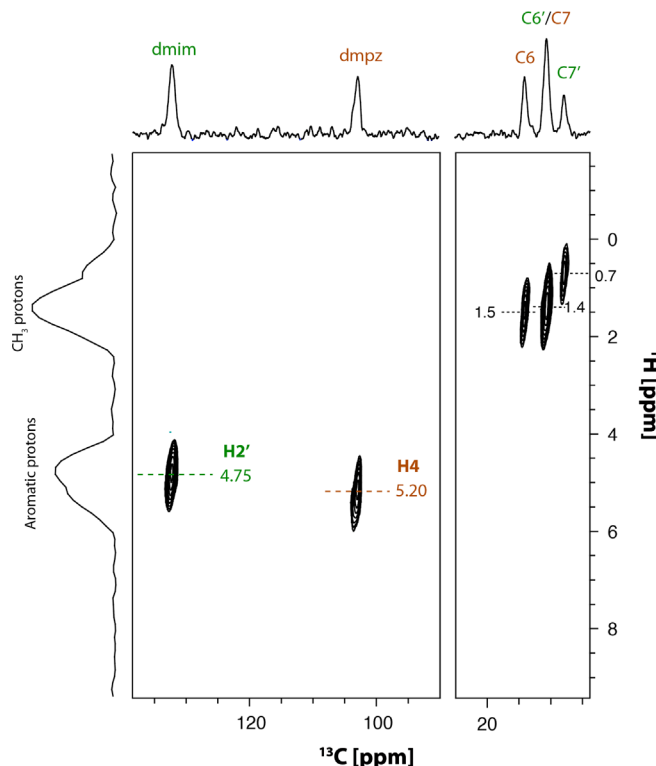


**Fig. 9.** 2D  $^1\text{H}$ - $^{13}\text{C}$  PRESTO-HETCOR spectrum of I recorded at  $B_0=9.4$  T and a MAS rate of 10 kHz. The acquisition parameters are the following: 64  $t_1$  points with 48 scans each were acquired along the F1 dimension; total mixing time of 177.8  $\mu\text{s}$  for the two RN blocks; dwell time in F1 of 137.6  $\mu\text{s}$  equivalent to two wDUMBO $_{\times \times}$  supercycles.

protons are expected to appear at  $\delta_{\text{H}}=1.3$  ppm according to Table 1).

The 2D  $^1\text{H}$ - $^{13}\text{C}$  LG-CP HETCOR experiment is used to determine short- and long-range  $^1\text{H} \dots ^{13}\text{C}$  heteronuclear proximities. The LG-CP transfer allows to obtain correlations with better selectivity compared to CP by quenching  $^1\text{H}$ - $^1\text{H}$  spin diffusion during the spin-lock  $^1\text{H}$  pulse [74–78]. The LG-CP experiment becomes particularly interesting and informative in accessing long-range  $^1\text{H} \dots ^{13}\text{C}$  correlations with reduced proton spin diffusion effects

that would otherwise mask the observation of long-range correlations.

To obtain insight on the relative molecular orientation between dmpz and dmim in the crystal packing of I,  $^1\text{H}$ - $^{13}\text{C}$  LG-CP HETCOR spectra were recorded at different mixing times (Fig. 10). The spectra show that a cross-peak appears between the H2' aromatic proton (dmim, dashed green line) and the C4 aromatic carbon of dmpz, suggesting that these atoms are in close proximity. The cross-peak observed at ca.  $\delta_{\text{H}}=5.2$  ppm and ca.  $\delta_{\text{C}}=104$  ppm refers to the directly attached C4-H<sub>dmpz</sub> atoms. In addition, two cross-peaks (indicated with circles) clearly vanish when the LG-CP contact time is reduced (from 2 to 0.5 ms, Fig. 10a and b): the H2'...C5' and H4...C5' aromatic cross-peaks are no longer present (orange circle), indicating that the C4 of dmpz is not in close contact to the C5' of dmim (see Fig. 4). This observation is consistent with the previous discussion and in agreement with the relative orientations between the two molecules described by the final PXRD crystal structure of I (Section 3.1). Another example of a cross-peak disappearing at shorter mixing times (marked with purple circles) involves the proximity of methyl protons to the C4 carbon (CH group) which is somewhat more difficult to explain as CH<sub>3</sub> groups are usually mobile and the interpretation of the 2D HETCOR spectrum would require variable temperature measurement to check the influence of CH<sub>3</sub> mobility in the cross peak intensity (not performed in this work). The same type of information is obtained comparing the 2D  $^1\text{H}$ - $^{13}\text{C}$  LG-CP HETCOR recorded with a mixing time of 0.2 ms and the 2D  $^1\text{H}$ - $^{13}\text{C}$  PRESTO-HETCOR, as both spectra only show the correlations between directly bonded C-H pairs (cp. Figs. 9 and 10c).

The 2D  $^1\text{H}$ - $^1\text{H}$  DQ-SQ experiment provides information regarding intermolecular contacts based on  $^1\text{H} \dots ^1\text{H}$  proximities. However, assessing  $^1\text{H} \dots ^1\text{H}$  distances in rigid solids through dipolar couplings poses several well-known difficulties and some pioneering work toward this direction has been reported [79].  $^1\text{H}$ - $^1\text{H}$  DQ MAS spectroscopy combines  $^1\text{H}$  CS resolution and information on  $^1\text{H}$ - $^1\text{H}$  dipolar interactions by employing dipolar recoupling pulse sequences for DQ generation in conjunction with fast MAS for  $^1\text{H}$  resolution enhancement [80,81]. The observation of individual DQ signals, in DQ spectra, implies the existence (or persistence) of a dipole-dipole coupling,  $D_{ij}$ , between the pair of nuclei on the time scale of the experiment (typically 10–100  $\mu\text{s}$ ). The absence of a DQ signal indicates a lack of the respective dipolar coupling

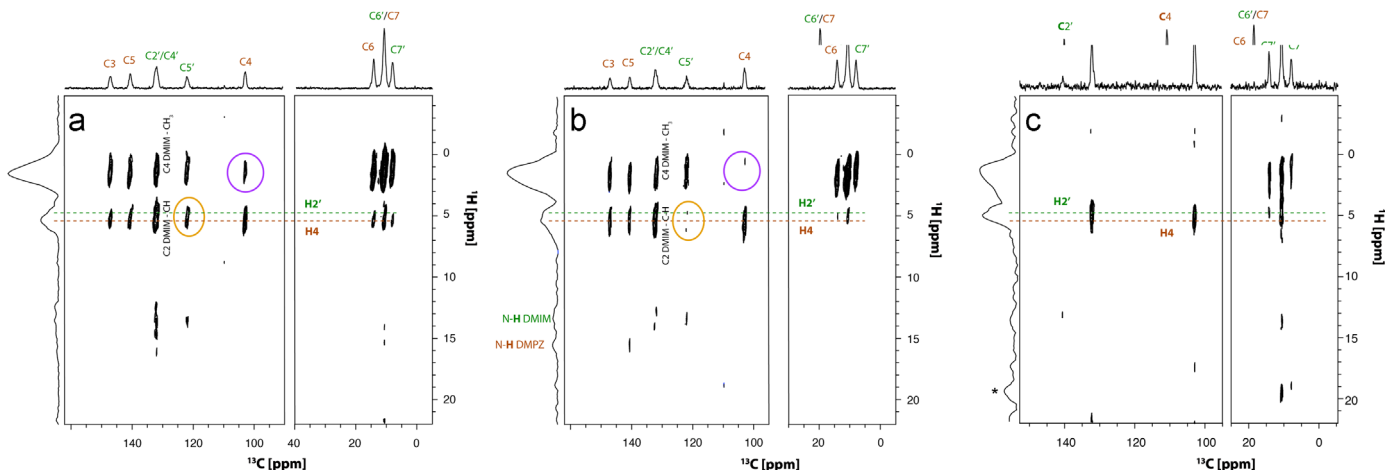


**Fig. 10.** 2D  $^1\text{H}$ - $^{13}\text{C}$  LG-CP HETCOR spectrum of **I** recorded at  $B_0=9.4$  T and a MAS rate of 10 kHz. The acquisition parameters are the following: 64  $t_1$  points with 16 scans each were acquired along the F1 dimension; dwell time in F1 of 140  $\mu\text{s}$  equivalent to two wDUMBO $_{x,-x}^x$  supercycles. Different contact times for the LG-CP were recorded, namely (a) 2000  $\mu\text{s}$ , (b) 500  $\mu\text{s}$  and (c) 200  $\mu\text{s}$ . The \* denotes a CRAMPS decoupling artifact and not a real peak. (For interpretation of the references to color in this figure legend, the reader is referred to the web version of this article.)

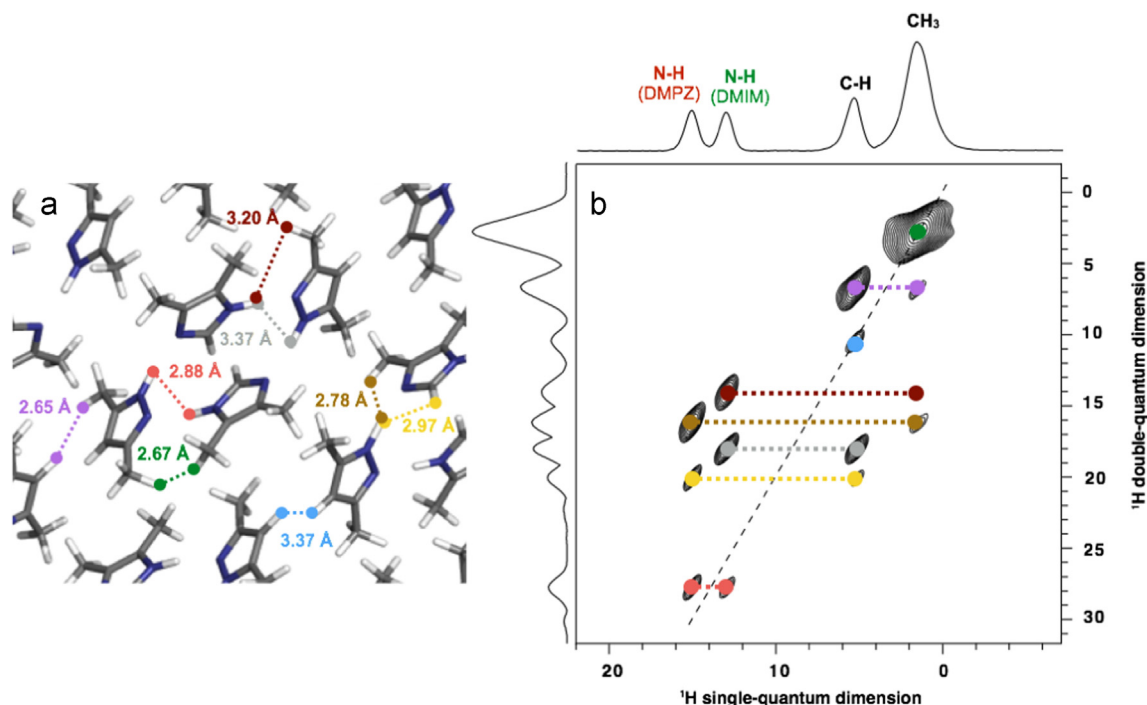


**Fig. 11.** (a) Crystal structure scheme illustrating the intermolecular contacts, with corresponding distances, of correlations highlighted in the (b) 2D  $^1\text{H}$ - $^1\text{H}$  DQ-SQ CRAMPS spectrum of **I** recorded at  $B_0=16.4$  T and MAS rate of 26 kHz. 156  $t_1$  points with 32 scans each were acquired along the F1 dimension; the DQ excitation and reconversion time was set to 76.8  $\mu\text{s}$ . Distances indicated in the scheme correspond to the shortest distances found in the structure for each indicated pair of protons. (For interpretation of the references to color in this figure legend, the reader is referred to the web version of this article.)

(approximately meaning that  $D_{ij}/2\pi < 2$  kHz), which can either be due to long-distance contacts (typically  $> 3.5$  Å) [80,82–84] or, in case of dynamic solids, the presence of fast local molecular dynamics on time scales  $< 100$   $\mu\text{s}$  [85]. To efficiently study proton rich materials such as organic solids this experiment has been usually combined with  $^1\text{H}$  CRAMPS decoupling [86–88], in both F1 and F2 dimensions thus yielding high-resolution  $^1\text{H}$  spectra. However, the use of  $^1\text{H}$  CRAMPS decoupling in 2D  $^1\text{H}$ - $^1\text{H}$  DQ-SQ spectra, shown in this work, yielded a spectrum (Fig. S3 in ESI) where the 28.4 ppm DQ peak, formed due to the proximity of N-H<sub>dmm</sub> and N-H<sub>dmpz</sub> ( $d_{\text{H}\cdots\text{H}}=2.88$  Å), unexpectedly “vanish”. To overcome this issue 2D  $^1\text{H}$ - $^1\text{H}$  DQ-SQ spectrum was performed at high-field (700 MHz) without the use of CRAMPS decoupling. This DQ peak is now present showing that the use of  $^1\text{H}$  DQ CRAMPS

experiments require some caution to be employed as a possible distance restraint tool.

The two types of N-H protons present in **I** (Fig. 11) show DQ correlations with CH<sub>3</sub> protons at  $\delta_{\text{DQ}}=14.4$  ppm and  $\delta_{\text{DQ}}=16.4$  ppm, expected due to the  $^1\text{H}\cdots{}^1\text{H}$  distance of less than 3.5 Å involving imidazole···imidazole, pyrazole···pyrazole and between pyrazole···imidazole rings (**dmim**···**dmpz**). In addition, there are also correlations between the N-H protons and the aromatic protons  $\delta_{\text{DQ}}=18.4$  ppm and  $\delta_{\text{DQ}}=20.4$  ppm, also expected as the distance between C-H and N-H protons is between 3 and 3.2 Å. The absence of peaks along the diagonal involving proximities of the chemically equivalent N-H resonances (expected at around  $\delta_{\text{DQ}}=26.4$  ppm and  $\delta_{\text{DQ}}=30.4$  ppm) indicates that equivalent N-H protons (i.e., N<sub>dmpz</sub>-H and H-N<sub>dmpz</sub>; N<sub>dmm</sub>-H

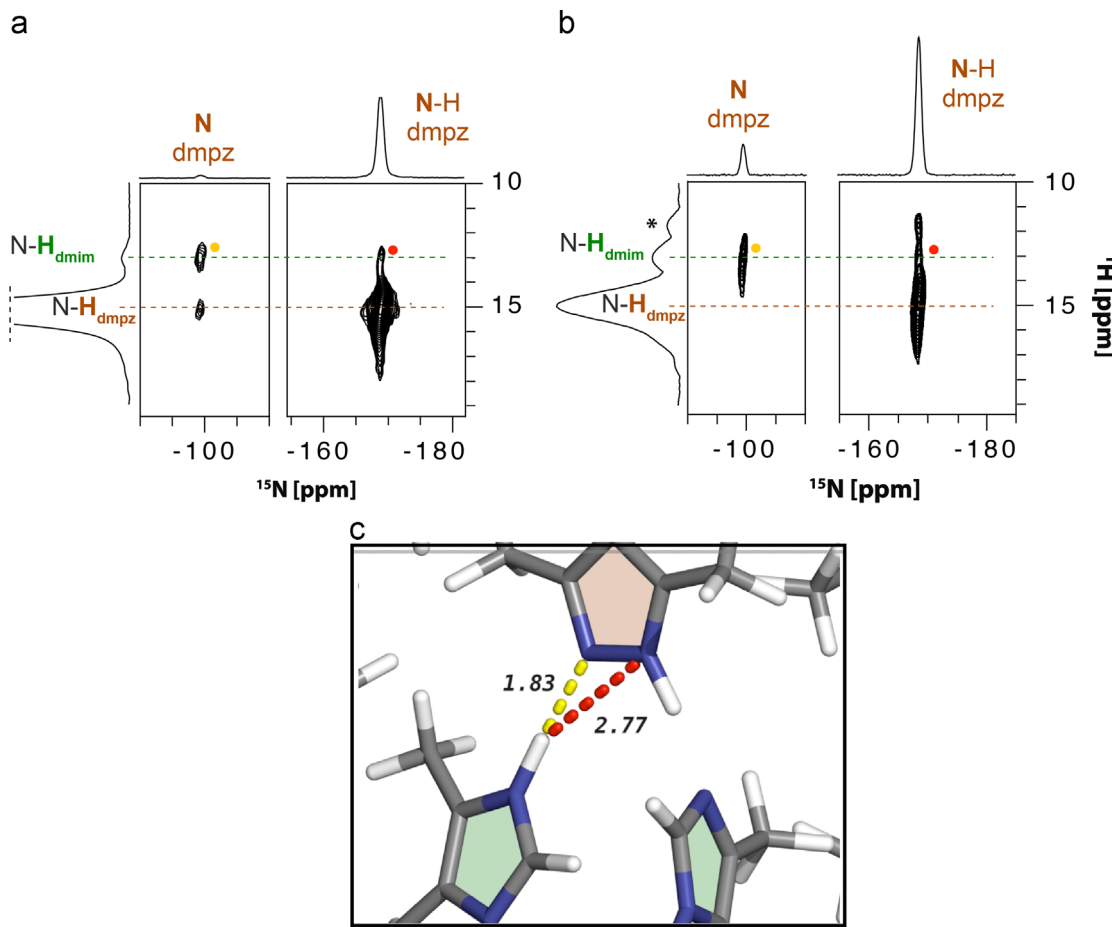


**Fig. 12.** (a) 2D  $^1\text{H}$ - $^{15}\text{N}$  CP HETCOR spectrum of **I** recorded at  $B_0 = 16.4 \text{ T}$ , with a MAS rate of 25 kHz and 1.0 ms mixing time. The acquisition parameters are the following: 217  $t_1$  points with 16 scans each were acquired along the F1 dimension; (b) 2D  $^1\text{H}$ - $^{15}\text{N}$  LG-CP HETCOR spectrum of **I** recorded at  $B_0 = 9.4 \text{ T}$ , with a MAS rate of 10 kHz and 0.5 ms mixing time. The acquisition parameters are the following: 64  $t_1$  points with 16 scans each were acquired along the F1 dimension; dwell time in F1 of 70  $\mu\text{s}$  equivalent to one wDUMBO $_{\text{xx}}$  supercycle; (c) part of the crystal structure highlighting the intermolecular contacts observed in both spectra: N<sub>dmpz</sub>···H-N<sub>dmim</sub> in yellow, 1.83 Å and H-N<sub>dmpz</sub>···H-N<sub>dmim</sub> in red, 2.77 Å. The \* denotes a CRAMPS decoupling artifact and not a real peak, which was confirmed by its absence when recorded in the same conditions but without CRAMPS decoupling. The same CP or LG-CP mixing times were employed in both 2D spectra. (For interpretation of the references to color in this figure legend, the reader is referred to the web version of this article.)

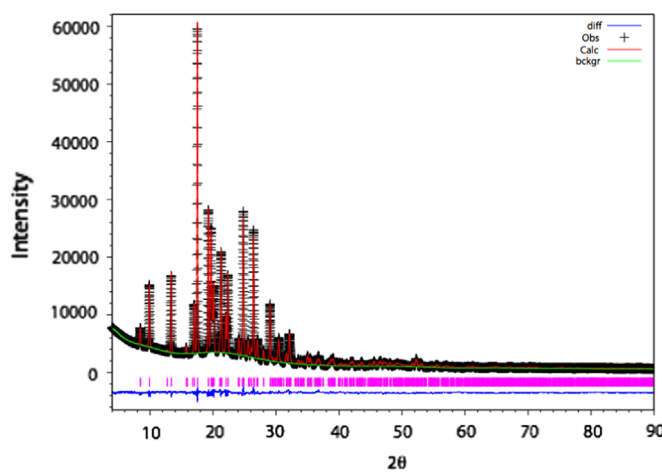


**Fig. 13.** Final Rietveld refinement for cocrystal **I**, showing the experimental (black + marks), calculated (red solid line), difference (blue solid line) and background (green solid line) PXRD profiles. (For interpretation of the references to color in this figure legend, the reader is referred to the web version of this article.)

and H-N<sub>dmim</sub>) are not sufficiently close in space to generate DQ coherences and are therefore not visible in Fig. 11. In the other hand, H-N<sub>dmpz</sub> and H-N<sub>dmim</sub> protons are close enough (2.88 Å; see

left side structure representation in Fig. 11) to contribute with a DQ crosspeak at 28.4 ppm. This information could be particularly important to discriminate between different candidate PXRD structure models.

The remaining strong correlations provide little relevant information, since they arise from the dipolar couplings among CH<sub>3</sub> groups (diagonal cross-peak at  $\delta_{\text{DQ}} = 3.2 \text{ ppm}$ ), CH aromatic protons ( $\delta_{\text{DQ}} = 10.4 \text{ ppm}$ ) and between the CH<sub>3</sub> groups and aromatic CH protons ( $\delta_{\text{DQ}} = 6.8 \text{ ppm}$ ).

In order to complete the NMR study on this system, 2D  $^1\text{H}$ - $^{15}\text{N}$  HETCOR experiments were also performed. Three correlations are observed in the spectrum of Fig. 12b, namely correlations between N<sub>dmpz</sub>···H<sub>dmim</sub>-N (yellow dot corresponding to NH hydrogen bond distance of 1.83 Å indicated by yellow dashed lines in Fig. 12c), H<sub>dmpz</sub>-N···H<sub>dmim</sub>-N (red dot corresponding to a N···H distance of 2.77 Å indicated by red dashed lines in Fig. 12c) and finally the strongest N···H correlation due to a directly bonded N-H pair (N<sub>dmpz</sub>-H, observed at 15 ppm for  $^1\text{H}$  and -170 ppm for  $^{15}\text{N}$ ). The  $^{15}\text{N}$  resonances of **dmim** are not observable in the spectrum since the sample used to perform this experiment is cocrystal **I** formed by regular **dmim** and  $^{15}\text{N}$ -enriched **dmpz**, following the protocol described in Section 2.

As illustrated in the scheme (Fig. 12c), the distance between N<sub>dmpz</sub> and H<sub>dmim</sub>-N is shorter (1.83 Å) than the distance between H<sub>dmpz</sub>-N and H<sub>dmim</sub>-N (2.77 Å), justifying the difference in

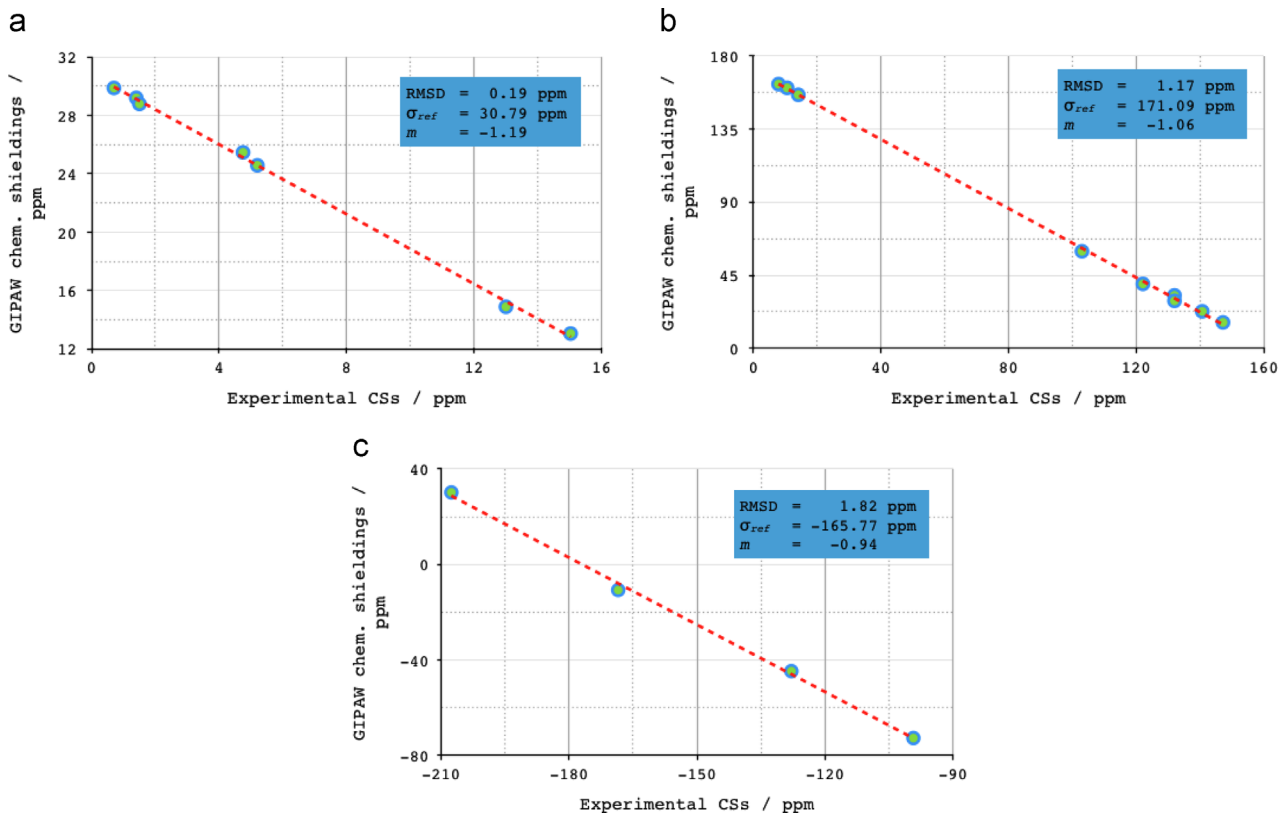


**Fig. 14.** GIPAW chemical shieldings vs measured CSs for (a)  $^1\text{H}$  (b)  $^{13}\text{C}$  and (c)  $^{15}\text{N}$ , along with the corresponding conversion parameters ( $m$  and  $\sigma_{ref}$  in Eq. 1) and the root-mean-square deviation (RMSD) between the measured and the calculated CSs.

intensities observed for the two correlations. Apart from the intermolecular correlations described before, intramolecular contacts are also observed in Fig. 12a ( $^1\text{H}$ - $^{15}\text{N}$  CP HETCOR), namely between the NH nitrogen of **dmpz** (N1) and its corresponding proton, observed at  $\delta_{\text{H}}=15$  ppm and  $\delta_{\text{N}}=-168.5$  ppm; and intramolecular contacts involving the  $\text{N}-\text{H}_{\text{dmpz}} \cdots \text{N}_{\text{dmpz}}$  contact ( $d_{\text{NH} \cdots \text{N}} \sim 2.11 \text{ \AA}$ ), observed at  $\delta_{\text{H}}=15$  ppm and  $\delta_{\text{N}}=-99.3$  ppm.

Using an LG-CP transfer in the 2D  $^1\text{H}$ - $^{15}\text{N}$  HETCOR (Fig. 12b), eliminated the cross peak appearing at  $\delta_{\text{H}}=15$  ppm and  $\delta_{\text{N}}=-99.3$  ppm, as cross peaks due to  $\text{N} \cdots \text{H}$  contacts not belonging to N-H bondings are efficiently suppressed during the employed mixing time.

#### 3.4. PXRD structure refinement and structure validation aided by SSNMR and GIPAW-DFT chemical shift calculations

Fig. 13 illustrates the comparison between the experimental and calculated XRD powder patterns, based on the refinement of the structure model built taking into account NMR data reported in Section 3.3. The almost perfect agreement between experimental and calculated PXRD data helps in validating the proposed crystal structure. All the procedure to refine the structure model is described at the experimental section.

The proposed structure of **I** was further refined through computational methods, *i.e.*, re-optimized at the DFT level and the proton positions were relaxed. The  $^1\text{H}$ ,  $^{13}\text{C}$  and  $^{15}\text{N}$  CSs of this structure were calculated using the GIPAW formalism and compared with the experimental CSs for final structure validation (Fig. 14 and Table 1). Indeed, all the CSs calculated for the geometry-optimized structure are in agreement with the corresponding experimental SSNMR data (see Section 3.3). The comparison of CSs calculated using the GIPAW method for the crystal

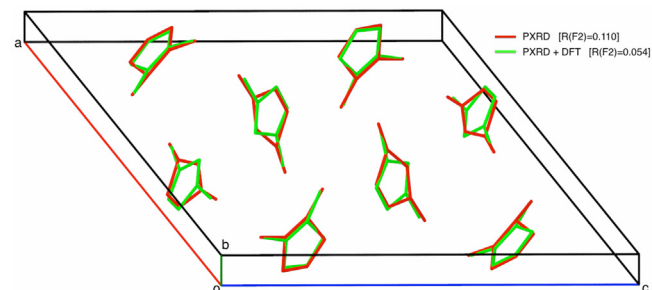


**Fig. 15.** Overlay between cocrystal **I** crystal structures using PXRD refinement only (red) and PXRD+DFT refinement (green). Hydrogen atoms are not shown for the sake of clarity. (For interpretation of the references to color in this figure legend, the reader is referred to the web version of this article.)

structure of **I** determined from PXRD data represents a robust and independent validation of the structure.

We have also compared the figure-of-merit [ $R(F^2)$ ] of cocrystal **I** at different refinement conditions to better visualize what is the impact of DFT refinement in the final structure, which can be directly compared to single crystal X-ray diffraction analysis and, thus, it is model-dependent only. Structure **I** was refined to an  $R$ -factor of  $R(F^2) \sim 11\%$  using PXRD methods only. After DFT geometry optimization of all atom positions (including hydrogens) the structure presented an  $R$ -factor of  $R(F^2)=5.4\%$  as indicated in Table S1. This indicates a drop in about 5.6% in  $R(F^2)$  due to the use of DFT+NMR approach to provide the adequate locations of protons and correct ring geometries. Fig. 15 shows the overlap of **I** resulting from PXRD refinement without and with DFT full atom geometry optimization.

To further enhance the importance of using DFT+NMR data to complement PXRD we compared the high theta angle region of two Rietveld refinement plots corresponding to the final refined

structure (Fig. 16a, a zoom in of Fig. 14) and the same structure without hydrogen atoms (Fig. 16b). Comparing both figures it is clear that absence of hydrogens will yield a worse fit, which is translated in a  $R(F^2)$  drop of about 2.3% (from 5.4% to 7.7%).

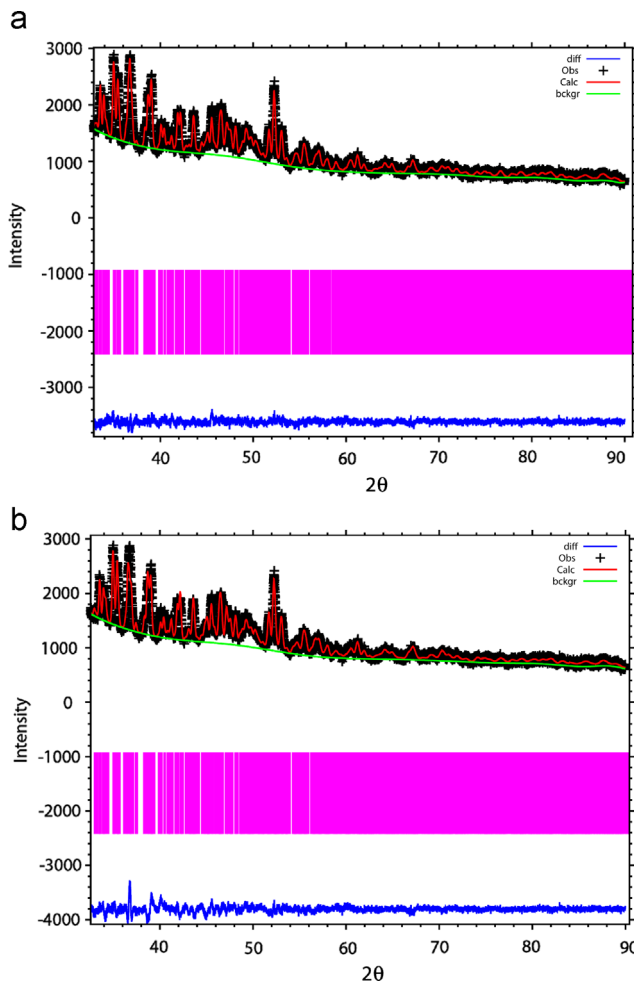


**Fig. 16.** Rietveld refinement for cocrystal I (a) without and (b) with hydrogen positioned using DFT refinement. The different line colors have the following meaning: experimental (black+marks), calculated (red solid line), difference (blue solid line) and background (green solid line) PXRD profiles. The  $R(F^2)$ -factors obtained for (a) and (b) are respectively, 5.4% and 7.7%. (For interpretation of the references to color in this figure legend, the reader is referred to the web version of this article.)

### 3.5. Sensing crystal packing interactions comparing solution vs solid-state NMR chemical shifts

**Table 2** summarizes the experimental solution and solid-state  $^1\text{H}$  NMR CSs of all proton sites in **dmpz** and **dmim**, highlighting the packing influence on the  $^1\text{H}$  NMR CS (the packing influence  $\Delta\delta$  – is defined as the difference between  $\delta_{\text{solid}}$  and  $\delta_{\text{solution}}$ ). As expected, the highest packing effects ( $\Delta\delta \sim 5.1$  and 3.9 ppm for **dmpz** and **dmim**, respectively) are observed for the CS of protons involved in the strong N-H $\cdots$ N H-bonds. However, a high-field upshift ( $\sim 2.7$  ppm) of the  $^1\text{H}$  CS of the C-H group of **dmim** is observed, denoting the ring-proton effects present in this resonance due to the formation of C-H $\cdots\pi$  interactions between all the molecules of **dmim** within the crystal [89]. The estimated packing effects of the  $^1\text{H}$  atom involved in the C-H $\cdots\pi$  interaction found for **dmim** are consistent with our previous quantification for the case of ciprofloxacin, corroborated with *in silico* computer simulations [12].

In contrast to strong/moderate H-bonds with energies of  $-5$  to  $-40$  kcal/mol, C-H $\cdots\pi$  contacts have a negligible impact ( $-1$  to  $-5$  kcal/mol), and little is known about their structural role in solids. They are often neglected when discussing molecular assemblies [26]. Recently, however, C-H $\cdots\pi$  contacts have been identified in protein-pharmaceutical complexes [23,90].

## 4. Conclusions

The crystal structure of a new powdered pyrazole $\cdots$ imidazole cocrystal was determined and described based on the data retrieved from PXRD, SSNMR and computational methods. The complete resonance assignment of the cocrystal was achieved combining high-resolution multinuclear NMR and GIPAW-DFT based CS calculations. The SSNMR methodology implemented in this work provided a set of experiments sensitive to the relative orientation between the two molecules (**dmpz** and **dmim**) forming the cocrystal. This contribution presents sophisticated 1D and 2D high-resolution  $^1\text{H}$ -based methods of high utility to probe packing interactions in small organic molecules. The newly presented cocrystal structure presents an atypical helical

**Table 2**  
Quantification of crystal packing interactions in experimental  $^1\text{H}$  NMR CSs.

Atom label	H-bond type	$\delta_{\text{solution}}$ (ppm) in isolated molecules	$\delta_{\text{solid}}$ (ppm) in cocrystal	$\Delta\delta$ (ppm) $\delta_{\text{solid}} - \delta_{\text{solution}}$ (packing influence)
<b>dmim</b>	C-H	C-H $\cdots\pi$	7.43	4.75
	CH <sub>3</sub> N-H	– N-H $\cdots$ N	2.17 9.12	1.48 13.00
<b>dmpz</b>	C-H	–	5.82	5.20
	CH <sub>3</sub> N-H	– N-H $\cdots$ N	2.27 9.95	1.44 15.03

supramolecular network of azole H-bonds stabilized by N–H···N and C–H···π interactions, yielding a final product more stable than the well-known H-bonded pyrazole trimer (**dmpz**). None of the other studied imidazole cocrystal former molecules (imidazole, 2-methylimidazole and 2,4(5)-dimethylimidazole) were able to disrupt the stable H-bonded **dmpz** trimer when combined with it. Quantification of crystal packing interactions was accessed through the comparison of <sup>1</sup>H CSs in the solid and solution (after dissolution of the cocrystal) phase. C–H···π interactions have shifted the proton resonance by ~2.7 ppm while strong N–H···N displaced the proton CSs up to ~5 ppm (Table 2). The work presented highlights the importance of combining methods in crystal structure determination of powders. Together with the *ab initio* CS calculations, the results from SSNMR enable the validation of the structure obtained by PXRD and DFT geometry optimization methods.

## Acknowledgments

We thank FCT, QREN, COMPETE, and EU for financial support and postdoc Grants for M.S. (SFRH/BPD/65978/2009), S.M.S. (SFRH/BPD/64752/2009) and A. A. B. (sponsored by the FCT project PTDC/QUIQUI/100998/2008). The Portuguese NMR Network (RNRMN) is acknowledged for granting access to the 18.8T NMR Bruker spectrometer at ITQB. FCT is also acknowledged for funding R&D Projects PTDC/QUIQUI/100998/2008, EXPL/QEQ-QFI/2078/2013 (COMPETE: COMP-01-0124-FEDER-041966) and PEst-C/CTM/LA0011/2011. Thanks are also given to the Ministerio de Economía y Competitividad of Spain (Projects CTQ2009-13129-C02-02 and CTQ2010-16122) and the Comunidad Autónoma de Madrid (Project MADRISOLAR2, ref. S2009/PPQ-1533). LM thanks FCT for the awarded development Grant (IF/01401/2013).

## Appendix A. Supporting information

Supplementary data associated with this article can be found in the online version at <http://dx.doi.org/10.1016/j.ssnmr.2014.12.005>.

## References

- [1] R.K. Harris, R.E. Wasylyshen, M.J. Duer, *NMR Crystallography*, John Wiley and Sons, Chichester, 2009.
- [2] E. Salager, G.M. Day, R. Stein, C.J. Pickard, B.N.D. Elena, L. Emsley, *J. Am. Chem. Soc.* 132 (2010) 2564–2566.
- [3] M. Baías, C.M. Widdifield, J. Dumez, H.P.G. Thompson, T.G. Cooper, E. Salager, et al., *Phys. Chem. Chem. Phys.* 15 (2013) 8069–8080.
- [4] M. Baías, J. Dumez, P.H. Svensson, S. Schantz, G.M. Day, L. Emsley, *J. Am. Chem. Soc.* 135 (2013) 17501–17507.
- [5] D.V. Dudenko, P.A. Williams, C.E. Hughes, O.N. Antzutkin, S.P. Velaga, S.P. Brown, et al., *J. Phys. Chem. C* 117 (2013) 12258–12265.
- [6] C.J. Pickard, F. Mauri, *Phys. Rev. B* 63 (2001) 245101.
- [7] J.R. Yates, C.J. Pickard, F. Mauri, *Phys. Rev. B* 76 (2007) 024401.
- [8] T. Charpentier, *Solid State Nucl. Magn. Reson.* 40 (2011) 1–20.
- [9] R.K. Harris, P. Hodgkinson, C.J. Pickard, J.R. Yates, V. Zorin, *Magn. Reson. Chem.* 45 (2008) S174–S186.
- [10] E.D.L. Smith, R.B. Hammond, M.J. Jones, K.J. Roberts, J.B.O. Mitchell, S.L. Price, et al., *J. Phys. Chem. B* 105 (2001) 5818–5826.
- [11] A. Webber, L. Emsley, R.M. Claramunt, S.P. Brown, *J. Phys. Chem. A* 114 (2010) 10435–10442.
- [12] L. Mafra, S.M. Santos, R. Siegel, I. Alves, F.A.A. Paz, D.V. Dudenko, et al., *J. Am. Chem. Soc.* 134 (2012) 71–74.
- [13] D.A. Middleton, X. Peng, D. Saunders, K. Shankland, W.I.F. David, A.J. Markvardsen, *Chem. Commun.* (2002) 1976–1977.
- [14] M. Aluas, C. Tripon, J.M. Griffin, X. Filip, V. Ladizhansky, R.G. Griffin, et al., *J. Magn. Reson.* 199 (2009) 173–187.
- [15] E. Salager, R. Stein, C.J. Pickard, B.N.D. Elena, L. Emsley, *Phys. Chem. Chem. Phys.* 11 (2009) 2610–2621.
- [16] A.S. Tatton, T.N. Pham, F.G. Vogt, D. Iuga, A.J. Edwards, S.P. Brown, *Mol. Pharm.* 10 (2013) 999–1007.
- [17] M. Khan, V. Enkelmann, G. Brunklaus, *CrystEngComm* 13 (2011) 3213–3223.
- [18] C.B. Åakeröy, D.J. Salmon, *CrystEngComm* 7 (2005) 439–448.
- [19] K.S. Kim, P. Tarakeshwar, J.Y. Lee, *Chem. Rev.* 100 (2000) 4145–4186.
- [20] S.K. Seth, P. Manna, N.J. Singh, M. Mitra, A.D. Jana, A. Das, et al., *CrystEngComm* 15 (2013) 1285–1288.
- [21] J.C. Ma, D.A. Dougherty, *Chem. Rev.* 97 (1997) 1303–1324.
- [22] D. Kim, S. Hu, P. Tarakeshwar, K.S. Kim, *J. Phys. Chem. A* 107 (2003) 1228–1238.
- [23] M. Nishio, Y. Umezawa, J. Fantini, M.S. Weiss, P. Chakrabarti, *Phys. Chem. Chem. Phys.* 16 (2014) 12648–12683.
- [24] M. Nishio, M. Hirota, Y. Umezawa, The CH/π interaction: evidence, nature, and consequences, 1998.
- [25] H.-J. Schneider, *Angew. Chem. Int. Ed.* 48 (2009) 3924–3977.
- [26] S. Tsuzuki, *Interactions with Aromatic Rings*, Springer-Verlag, Berlin/Heidelberg, 2005.
- [27] P. Sozzani, A. Comotti, S. Bracco, R. Simonutti, *Angew. Chem. Int. Ed.* 43 (2004) 2792–2797.
- [28] P. Sozzani, A. Comotti, S. Bracco, R. Simonutti, *Chem. Commun.* 0 (2004) 768–769.
- [29] S. Tsuzuki, *Annu. Rep. Prog. Chem. Sect. C: Phys. Chem.* 108 (2012) 69–95.
- [30] J. Elguero, P. Goya, N. Jagerovic, A. Silva, Pyrazoles as drugs: facts and fantasies, in: O.A. Attanasi, D. Spinelli (Eds.), *Targets in Heterocyclic Systems – Chemistry and Properties*, Italian Society of Chemistry, Roma, 2002, pp. 52–98.
- [31] R. Pérez-Fernández, P. Goya, J. Elguero, *Arkivoc* 2 (2014) 233–293.
- [32] A. Verma, S. Joshi, D. Singh, J. Chem. 2013 (2013) 1–12.
- [33] L. Zhang, X.-M. Peng, G.L.V. Damu, R.-X. Geng, C.-H. Zhou, *Med. Res. Rev.* 34 (2013) 340–437.
- [34] A. Baldy, J. Elguero, R. Faure, M. Pierrot, *J. Am. Chem. Soc.* 107 (1985) 5290–5291.
- [35] F. Aguilar-Parrilla, G. Scherer, H.-H. Limbach, M.C. Foces-Foces, F.H. Cano, J.A. S. Smith, et al., *J. Am. Chem. Soc.* 114 (1992) 9657–9659.
- [36] O. Klein, F. Aguilar-Parrilla, J.M. Lopez, N. Jagerovic, J. Elguero, H.-H. Limbach, *J. Am. Chem. Soc.* 126 (2004) 11718–11732.
- [37] C. López, R.M. Claramunt, M.Á. García, J. Elguero, *Cent. Eur. J. Chem.* 2 (2004) 660–671.
- [38] R.H. Wiley, P.E. Hexner, *Org. Synth.* 4 (1963) 351.
- [39] R.M. Claramunt, C. López, M.Á. García, G.S. Denisov, I. Alkorta, J. Elguero, *New J. Chem.* 27 (2003) 734–742.
- [40] H. Bredereck, G. Theilig, *Chem. Ber.* 86 (1953) 88–96.
- [41] A. D'Sa, L.A. Cohen, J. Heterocycl. Chem. 28 (1991) 1819–1820.
- [42] D. Sakellariou, A. Lesage, P. Hodgkinson, L. Emsley, *Chem. Phys. Lett.* 319 (2000) 253–260.
- [43] B.M. Fung, A.K. Khitrin, K. Ermolaev, *J. Magn. Reson.* 142 (2000) 97–101.
- [44] X. Zhao, W. Hoffbauer, J. Gunne, M. Levitt, *Solid State Nucl. Magn. Reson.* 26 (2004) 57–64.
- [45] S. Paul, R.S. Thakur, M. Goswami, A.C. Sauerwein, S. Mamone, M. Concristre, et al., *J. Magn. Reson.* 197 (2009) 14–19.
- [46] D. Louér, M. Louér, *J. Appl. Cryst.* 5 (1972) 271–275.
- [47] A. Boultif, D. Louér, *J. Appl. Cryst.* 37 (2004) 724–731.
- [48] A. Altomare, C. Cuocci, C. Giacovazzo, A. Moliterni, R. Rizzi, N. Corriero, et al., *J. Appl. Cryst.* 46 (2013) 1231–1235.
- [49] T.A. Halgren, *J. Comput. Chem.* (1996).
- [50] A. Altomare, N. Corriero, C. Cuocci, A. Moliterni, R. Rizzi, *J. Appl. Cryst.* 46 (2013) 779–787.
- [51] R.A. Young, *Cryst. Res. Technol.* 30 (1995).
- [52] P. Thompson, D.E. Cox, J.B. Hastings, *J. Appl. Cryst.* 20 (1987) 79–83.
- [53] C.J. Howard, *J. Appl. Cryst.* 15 (1982) 615–620.
- [54] K. Shankland, M.J. Spillman, E.A. Kabova, D.S. Edgeley, N. Shankland, *Acta Cryst. C* 69 (2013) 1251–1259.
- [55] J.P. Perdew, K. Burke, M. Ernzerhof, *Phys. Rev. Lett.* 77 (1996) 3865–3868.
- [56] S.J. Clark, M.D. Segall, C.J. Pickard, P.J. Hasnip, M.I.J. Probert, K. Refson, et al., *Z. Kristallogr.* 220 (2005).
- [57] F.H. Allen, W. Motherwell, *Acta Crystallogr. Sect. B* 58 (2002) 407–422.
- [58] F.H. Allen, *Acta Crystallogr. B Struct. Sci.* 58 (2002) 380–388.
- [59] CSD version 5.34, updated May 2013. (<http://www.ccdc.cam.ac.uk>).
- [60] C.C. Foces-Foces, I. Alkorta, J. Elguero, *Acta Crystallogr. Struct. B* 56 (2000) 1018–1028.
- [61] C.J. Serpell, N.L. Kilah, P.J. Costa, V. Félix, P.D. Beer, *Angew. Chem. Int. Ed.* 49 (2010) 5322–5326.
- [62] C.J. Serpell, P.D. Beer, *Cryst. Growth Des.* 13 (2013) 2866–2871.
- [63] F. Bonati, Gazz. Chim. Ital. 119 (1989) 291 (~200).
- [64] P. Fantucci, V. Valenti, *J. Chem. Soc. Dalton Trans.* 0 (1992) 1981–1988.
- [65] C. de L.C. Foces-Foces, A.L. Llamas-Saiz, R.M. Claramunt, C. López, J. Elguero, *J. Chem. Soc. Chem. Commun.* 0 (1994) 1143–1145.
- [66] A.L. Llamas-Saiz, C. de L.C. Foces-Foces, J. Elguero, *J. Mol. Struct.* 319 (1994) 231–260.
- [67] A.L. Llamas-Saiz, C.C. Foces-Foces, O. Mó, M. Yañez, E. Elguero, J. Elguero, *J. Comput. Chem.* 16 (1995) 263–272.
- [68] I. Alkorta, J. Elguero, B. Donnadieu, M. Etienne, J. Jaffart, D. Schagen, et al., *New J. Chem.* 23 (1999) 1231–1237.
- [69] R.M. Claramunt, C. López, M.A. García, M.D. Otero, M.R. Torres, E. Pinilla, et al., *New J. Chem.* 25 (2001) 1061–1068.
- [70] R.M. Claramunt, P. Cornago, Supramol. Chem. 18 (2006) 349–356.
- [71] I. Alkorta, G. Sánchez-Sanz, C. Trujillo, J. Elguero, R.M. Claramunt, *Arkivoc II* (2012) 85–106.
- [72] P. Cabido, R.M. Claramunt, F.J. Zúñiga, I. Alkorta, J. Elguero, Z. Kristallogr. (2015) (submitted for publication).

- [73] M. Sardo, R. Siegel, S.M. Santos, J. Rocha, J. Gomes, L. Mafra, *J. Phys. Chem. A* 116 (2012) 6711–6719.
- [74] V. Ladizhansky, S. Vega, *J. Am. Chem. Soc.* 122 (2000) 3465–3472.
- [75] V. Ladizhansky, S. Vega, *J. Chem. Phys.* 112 (2000) 7158.
- [76] J. Brus, A. Jegorov, *J. Phys. Chem. A* 108 (2004) 3955–3964.
- [77] M. Hong, X. Yao, K. Jakes, D. Huster, *J. Phys. Chem. B* 106 (2002) 7355–7364.
- [78] A. Ramamoorthy, C.H. Wu, S.J. Opella, *J. Magn. Reson.* 140 (1999) 131–140.
- [79] S.P. Brown, H.W. Spiess, *Chem. Rev.* 101 (2001) 4125–4156.
- [80] I. Schnell, H.W. Spiess, *J. Magn. Reson.* 151 (2001) 153–227.
- [81] I. Schnell, S.P. Brown, H.Y. Low, H. Ishida, H.W. Spiess, *J. Am. Chem. Soc.* 20 (1998) 11784.
- [82] H. Geen, J.J. Titman, J. Gottwald, H.W. Spiess, *Chem. Phys. Lett.* 2227 (1994) 78–86.
- [83] S.P. Brown, *Prog. Nucl. Mag. Res. Spectrosc.* 50 (2007) 199–251.
- [84] H.W. Spiess, *eMagRes* 1 (2012) 109–126. <http://dx.doi.org/10.1002/9780470034590.emrstm0133>.
- [85] G.R. Goward, M.F.H. Schuster, D. Sebastiani, I. Schnell, H.W. Spiess, *J. Phys. Chem. B* 106 (2002) 9322–9334.
- [86] P.K. Madhu, E. Vinogradov, S. Vega, *Chem. Phys. Lett.* 394 (2004) 423–428.
- [87] L. Mafra, J. Gomes, J. Trébosc, J. Rocha, J. Amoureaux, *J. Magn. Reson.* 196 (2009) 88–91.
- [88] L. Mafra, R. Siegel, C. Fernandez, D. Schneider, F. Aussena, J. Rocha, *J. Magn. Reson.* 199 (2009) 111–114.
- [89] A. Caballero, F. Zapata, L. González, P. Molina, I. Alkorta, J. Elguero, *Chem. Commun.* 50 (2014) 4680–4682.
- [90] G. Tóth, S.G. Bowers, A.P. Truong, G. Probst, *Curr. Pharm. Des.* 13 (2007) 3476–3493.